

Supplementary Materials for

The reinvigoration of the Southern Ocean carbon sink

Peter Landschützer,* Nicolas Gruber, F. Alexander Haumann, Christian Rödenbeck,
Dorothee C. E. Bakker, Steven van Heuven, Mario Hoppema, Nicolas Metzl, Colm
Sweeney, Taro Takahashi, Bronte Tilbrook, Rik Wanninkhof

*Corresponding author. E-mail: peter.landschuetzer@usys.ethz.ch

Published 11 September 2015, *Science* **349**, 1221 (2015)
DOI: 10.1126/science.aab2620

This PDF file includes:

Supplementary Text
Figs. S1 to S12
Tables S1 and S2
References

1 Neural network-based ocean $p\text{CO}_2$ product

1.1 Method Update

The surface ocean $p\text{CO}_2$ product used here is an updated and extended version of the previously published product (1). The most important change is the temporal extension of the estimation period to cover the period from 1982 through 2011. This required a modification of the input data used to interpolate the $p\text{CO}_2$ observations in space and time. In particular, we use the satellite-era (1998 through 2013) average chlorophyll (<http://www.globcolour.info>) monthly climatology as predictor field for each year before 1998, which has almost no effect in years before 1998 when being compared to estimates created without chlorophyll. The inclusion of chlorophyll, however, does affect the sink estimates in the later years of the analysis period while it reduces the residual spread, providing a first order indication that biology is a relevant driver for the Southern Ocean carbon cycle. We also use the climatological mixed layer depth (2) instead of the interannually varying one used in the past (1). This change also led to very small changes for the period after 1998, in comparison to the results presented previously (1).

Additionally, we smoothed our output using the spatial and temporal mean of each point's neighboring pixels both in time and space within the $3 \times 3 \times 3$ pixel neighborhood domain. While the smoothing does not affect the long term mean, the trend or basin scale interannual variabilities, it creates smoother (and arguably more realistic) transitions at province borders in data sparse regions, such as the Southern Ocean.

1.2 Data Sources

We obtain our neural network results by assigning the surface ocean data to biogeochemical provinces using common patterns of sea-surface temperature (SST) (3), sea-surface salinity (SSS) (4), climatological mixed layer depth (MLD) (2), and climatological sea-surface $p\text{CO}_2$ (5). SST, MLD, SSS as well as Globcolour-based chlorophyll-a (<http://www.globcolour.info>)

and the dry air mixing ratio of atmospheric CO₂ (xCO₂) from the GLOBALVIEW marine boundary layer product (6) are then used to establish the non-linear relationship between these predictors and the target $p\text{CO}_2$.

1.3 Residuals

We carried out a residual analysis of the two-step neural network technique in order to test for the robustness of our main finding, i.e., if the flux is subject to systematic biases. For five year temporal intervals the difference between the estimated $p\text{CO}_2$ values and the SOCAT observations (7) (neural network minus SOCAT; Fig. S1) reveals a random distribution with no sign of a temporal bias. While the first ten years describe the data-poorest periods, observations exist in all Southern Ocean sectors for half-decade periods. The residuals further reveal no systematic spatial pattern, i.e., no Southern Ocean sector is biased high or low throughout the entire spatial extent and all the time intervals considered here. The overall bias stays close to zero for each period indicating that trends are not caused by a systematic misfit. The root mean squared error (RMSE) is strongly influenced by the number of observations and the span of observed $p\text{CO}_2$ values, hence it stays lowest within the first decade.

We performed a second test by using data from the LDEOv2013 database (8), which are not included in the SOCATv2 database (Fig. S2). We perform the residual analysis for 10-year periods due to the sparsity of the available data. While we find larger mean differences and RMSE values within almost all periods, there is no indication that our method is subject to any systematic bias, in either space or time. In contrast to the first test, the data used here can be considered fully independent, as they have not been used to train the neural network. The results illustrate that although the neural network estimates show a larger bias in comparison to independent data, the overall bias still tends to be low.

Finally, we test our estimates for potential biases arising from the heterogeneous distribution

Table S1: Bias and root mean squared error (RMSE) between the neural network estimates and the SOCATv2 as well as the LDEOv2013 databases. Only those data from the LDEOv2013 database have been considered that are not included in SOCAT

| period | bias (SOCAT) | RMSE (SOCAT) | bias (LDEO) | RMSE (LDEO) |
|-----------|--------------|--------------|-------------|-------------|
| | [μatm] | [μatm] | [μatm] | [μatm] |
| 1982-1986 | -0.8 | 13.1 | 1.9 | 28.3 |
| 1987-1991 | -1.0 | 13.8 | 7.32 | 26.9 |
| 1992-1996 | 2.0 | 17.8 | -1.8 | 19.0 |
| 1997-2001 | 0.8 | 20.7 | 0.4 | 25.8 |
| 2002-2006 | 1.4 | 19.0 | 3.4 | 23.6 |
| 2007-2011 | 0.6 | 19.6 | -3.1 | 23.8 |

of surface ocean CO₂ observations. Therefore, we divide the Southern Ocean into sub-sectors, i.e the Pacific sector (160°E-60°W), the Atlantic sector (60°W-30°E) and an Indian sector 30°E-160°E, and calculate the residuals (neural network estimates minus observation) for each sector individually. We do this both for the SOCATv2 and LDEOv2013 datasets. Fig. S3 and S4 reveal that the mean bias stays small throughout each sector within each period, although for both data products the spread significantly increases with the amount of data, reflecting the substantial amount of unresolved noise in the data.

1.4 CO₂ flux calculation

We calculate the air-sea flux density (mol C · m⁻² · yr⁻¹) from

$$F_{\text{CO}_2} = k_{ex} \cdot (1 - f_{ice}) \cdot (p\text{CO}_2^{\text{sea}} - p\text{CO}_2^{\text{atm}})$$

with k_{ex} describing the gas transfer coefficient of CO₂. Here, the flux is defined positive when CO₂ is outgassed from the ocean, and negative when CO₂ is taken up by the ocean. The fluxes are scaled to the ice-free area of each pixel, using sea ice cover data (f_{ice}) (9). For the gas transfer velocity a quadratic formulation (10) is used, where we adjusted the scaling factor to reach a global mean transfer velocity of 16 cm hr⁻¹ to match a recent estimate using a different

wind product (11). The windspeeds are taken from the ERA-interim wind product (12)

2 Trends of air-sea fluxes and atmospheric CO₂

2.1 Trend calculation

Trends were calculated by firstly removing the climatological mean seasonal cycle from the timeseries. Secondly, a linear regression line was fit through the data and the slope of the linear regression line was used as the trend estimate. Furthermore, for testing purposes, trends have been calculated by removing the long term mean seasonal cycle via a 12-month running mean filter, but little difference was found in the use of the latter approach.

2.2 Annual-mean trends

To evaluate the trend signals we calculate the overall Southern Ocean trend (south of 35°S - see Table S2), for each property for the periods 1992 through 2001 and 2002 through 2011 (calculated as described in the section 2.1). We find that with one exception, all trends are statistically significant (within the 95% confidence interval; $p \leq 0.05$), confirming the proposed reduction of the carbon sink from 1992 through 2001 and the strengthening of the sink from 2002 through 2011.

2.3 Seasonal trends

Fig. S5 reveals that the trends identified in the main manuscript exist in both winter and summer, though with some regional differences. Summer trends, particularly in the high latitudes, are more variable due to the presence of biology and therefore are less significant.

Table S2: Linear trends in the CO₂ flux method, i.e. the mixed layer scheme method (*13*), the neural network method (SOM-FFN) (*1*), the expected ocean uptake based on atmospheric CO₂ (derived from the CCSM3 model simulation (*14*) and the atmospheric inversion (*15*) for the time periods 1992 through 2001 and 2002 through 2011. Bold numbers indicate significant trends within the 95% confidence interval ($p \leq 0.05$).

| | 1992-2001 | 2002-2011 | unit |
|--------------------------------|-------------------|-------------------|---|
| SOM-FFN | 0.46±0.07 | -0.70±0.10 | [PgC · yr ⁻¹ · dec ⁻¹] |
| MLS | 0.69±0.17 | -0.25±0.19 | [PgC · yr ⁻¹ · dec ⁻¹] |
| Atmospheric Inversion | 0.00±0.13 | -0.38±0.15 | [PgC · yr ⁻¹ · dec ⁻¹] |
| expected Southern Ocean uptake | | | |
| CCSM | -0.10±0.00 | -0.08±0.00 | [PgC · yr ⁻¹ · dec ⁻¹] |

2.4 Trends in sea ice and k_{ex}

Trends in k_{ex} do not strongly affect the trends we see in the Southern Ocean uptake flux. This is confirmed by Fig. S7 and S8. Fig. S7 shows the trends in sea-ice (9) and k_{ex} (calculated (*10, 16*) using wind speed (*12*), temperature (*3*) and salinity (*4*)) for the periods from 1992 through 2001 and 2002 through 2011 and Fig. S8 illustrates the integrated flux by keeping either component of the flux equation (k_{ex} or $\Delta p\text{CO}_2$) constant. While Fig. S7 suggests that the increase in the winds in the Pacific sector does increase k_{ex} , the total magnitude of this effect is damped by the cooling identified in the same basin. Hence, Fig. S8 reveals that when considering a climatological mean $\Delta p\text{CO}_2$, the Southern Ocean flux barely changes on interannual to decadal timescales and the flux is mainly determined by changes in $\Delta p\text{CO}_2$.

2.5 Distribution in anomalous years

Fig. S9 illustrates the annual mean air-sea $\Delta p\text{CO}_2$ (a-c) and air-sea flux density (d-f) for 3 selected anomalous years. We find a strong uptake of CO₂ by the Southern Ocean (south of 35°S). While in 1992 and 2011 the majority of the Southern Ocean describes a CO₂ uptake region, the 2001 pattern reveals a very symmetric outgassing in the high latitudes. The anomalous $\Delta p\text{CO}_2$

pattern are both visible in the mixed layer scheme and the neural network output as illustrated in Fig. S10.

3 Trends of potential drivers

3.1 Circulation and Ekman pumping

Decadal changes in mean sea level pressure and near surface (10 m) wind field, illustrated in Fig. 3, are based on ERA-Interim (12) reanalysis data. The Ekman pumping velocity w_E and the vertically integrated northward Ekman transport v_E were derived from the monthly mean of the instantaneous surface wind stress components τ^x and τ^y using the following definitions:

$$w_E = \frac{1}{\rho_0 f} \left(\frac{\partial \tau^x}{\partial y} - \frac{\partial \tau^y}{\partial x} \right),$$

and

$$v_E = \frac{1}{\rho_0 f} \tau^x,$$

where ρ_0 is the reference density of 1030 kg m^{-3} and f is the common Coriolis parameter, which varies with latitude. The results illustrate the different processes in the last decade of our analysis period, i.e., a northward movement of water masses in the Pacific sector in contrast to a southward movement of the water masses in the Atlantic sector (Fig. S11).

3.2 Satellite chlorophyll-a

To investigate the potential effect of trends in biology related changes in the sea-surface $p\text{CO}_2$, we calculate trends from the satellite based Globcolor chlorophyll-a product (<http://www.globcolour.info>; as described in section 2.1). The results (Fig. S12) show few areas where trends are significant, one of them being the Atlantic sector within our study region, where chlorophyll-a trends show a significant increase.

References and Notes

1. P. Landschützer, N. Gruber, D. C. E. Bakker, U. Schuster, *Global Biogeochemical Cycles* **28**, 927949 (2014).
2. C. de Boyer Montegut, G. Madec, A. S. Fischer, A. Lazar, D. Iudicone, *Journal of Geophysical Research* **109**, C12003 (2004).
3. R. W. Reynolds, N. A. Rayner, T. M. Smith, D. C. Stokes, W. Wang, *Journal of Climate* **15**, 1609 (2002).
4. S. A. Good, M. J. Martin, N. A. Rayner, *Journal of Geophysical Research: Oceans* **118**, 6704 (2013).
5. T. Takahashi, *et al.*, *Deep-Sea Research II* **56**, 554 (2009).
6. GLOBALVIEW-CO₂, Cooperative atmospheric data integration project - carbon dioxide, CD-ROM, NOAA ESRL, Boulder, Colorado [Also available on Internet via anonymous FTP to ftp.cmdl.noaa.gov, Path: ccg/co2/GLOBALVIEW] (2014).
7. D. C. E. Bakker, *et al.*, *Earth System Science Data* **6**, 69 (2014).
8. T. Takahashi, S. C. Sutherland, A. Kozyr, Global ocean surface water partial pressure of co₂ database: Measurements performed during 1957-2012 (version 2013). ornl/cdiac-160, ndp-088(v2013)., *Tech. rep.*, Carbon Dioxide Information Analysis Center, Oak Ridge National Laboratory, U.S. Department of Energy, Oak Ridge, Tennessee (2014).
9. N. A. Rayner, *et al.*, *Journal of Geophysical Research* **108**, 4407 (2003).
10. R. Wanninkhof, *Journal of Geophysical Research* **97**, 7373 (1992).
11. R. Wanninkhof, *et al.*, *Biogeosciences* **10**, 1983 (2013).

12. D. P. Dee, *et al.*, *Quarterly Journal of the Royal Meteorological Society* **137(656)**, 553 (2011).
13. C. Rödenbeck, *et al.*, *Biogeosciences* **11**, 4599 (2014).
14. H. D. Graven, N. Gruber, R. Key, S. Khatiwala, X. Giraud, *J. Geophys. Res.* **117**, C10005 (2012).
15. C. Rödenbeck, S. Houweling, M. Gloor, M. Heimann, *Atmos. Chem. Phys.* **3**, 1919 (2003).
16. R. F. Weiss, *Marine Chemistry* **2**, 203 (1974).

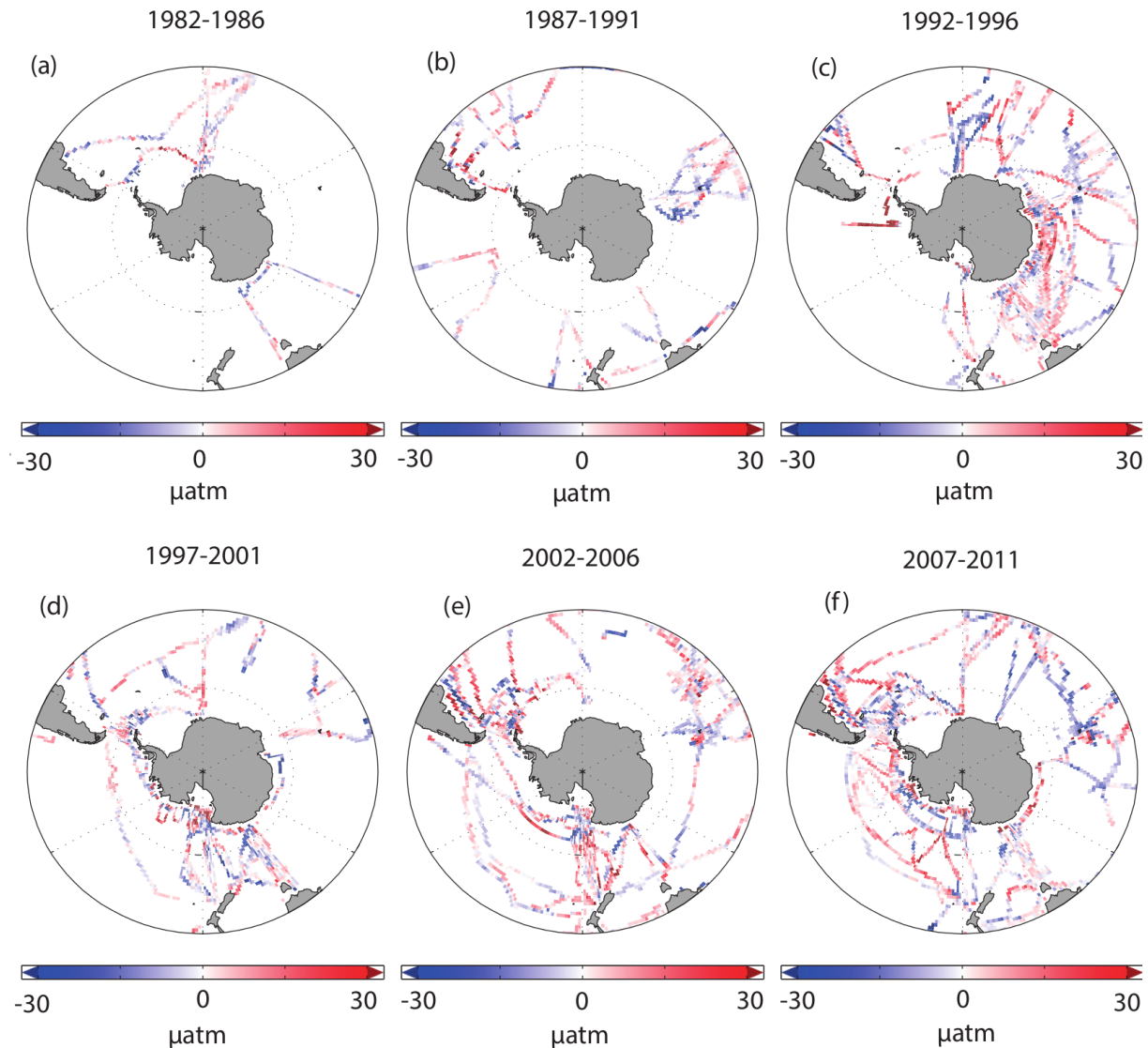


Figure S1: Residuals between the SOCATv2 gridded observations and the neural network $p\text{CO}_2$ estimates for the area south of 35°S . The analysis is presented for intervals of five years from 1982 onward (a-f) due to the sparsity of available observations.

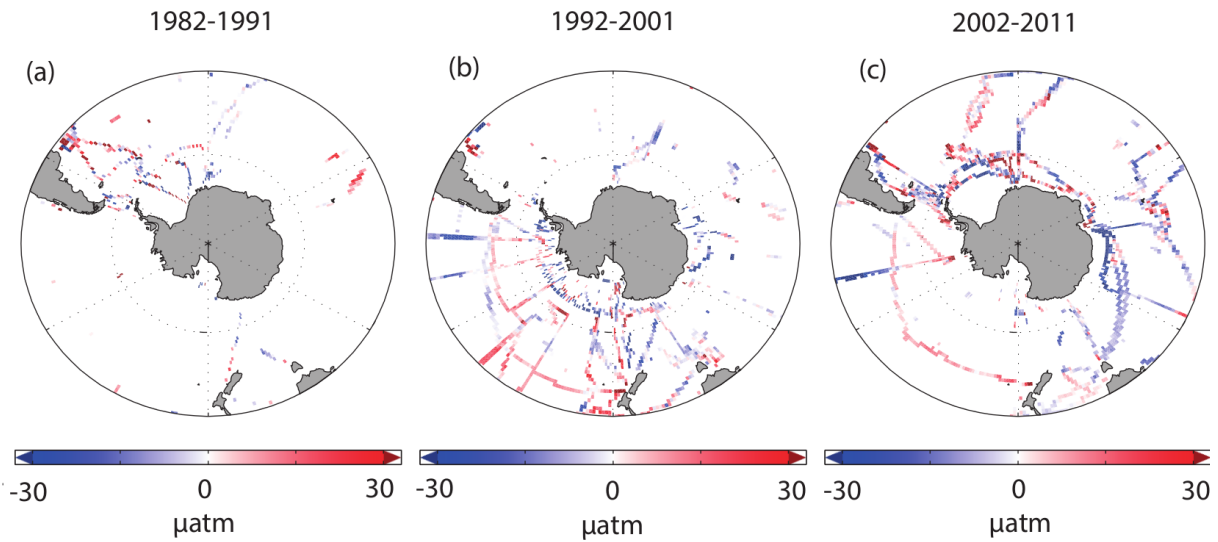


Figure S2: Residuals between the LDEOv2013 gridded observations, that are not included in SOCATv2 and the neural network $p\text{CO}_2$ estimates for the area south of 35°S . The analysis is presented for intervals of 10 years from 1982 onward (a-c) due to the sparsity of available observations.

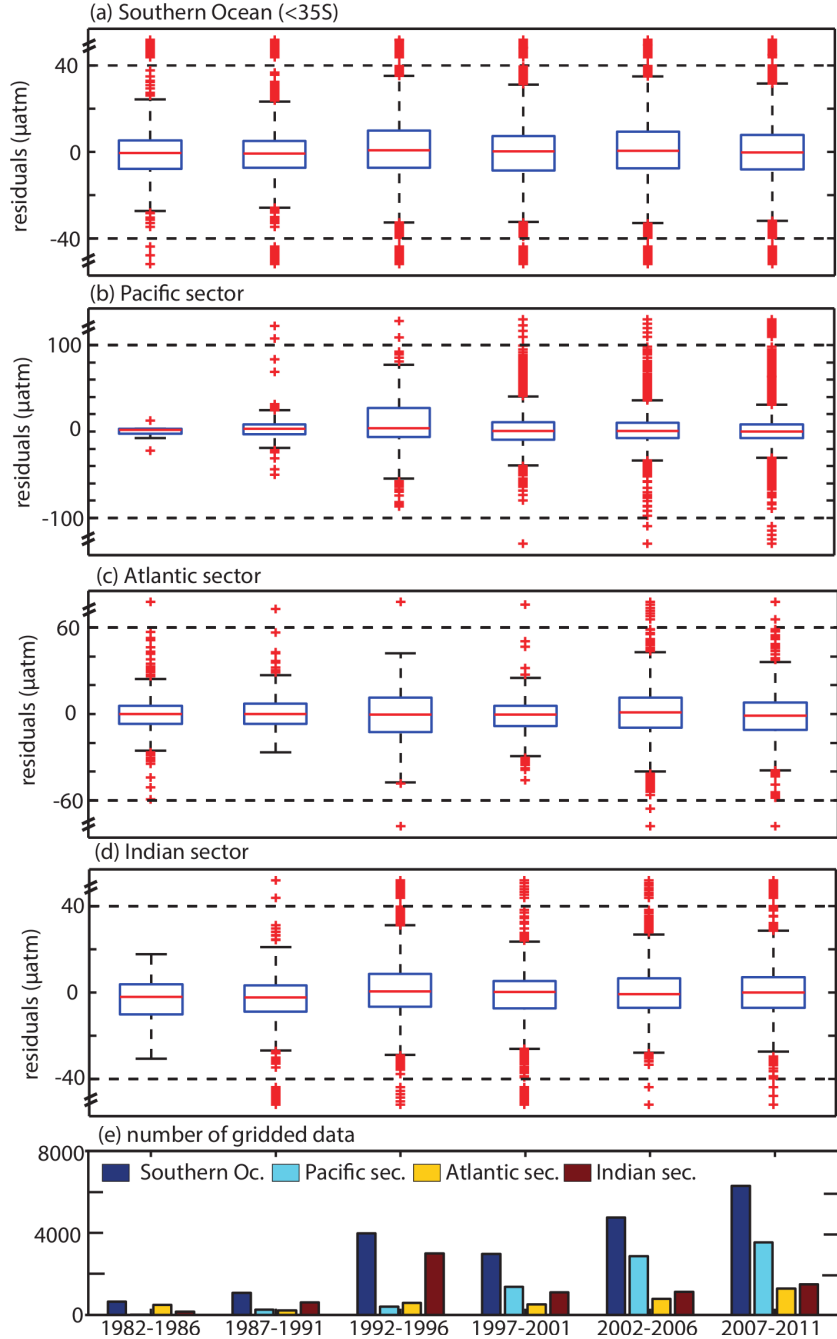


Figure S3: Box-whiskers plot of the residuals between the SOCATv2 gridded observations and the neural network $p\text{CO}_2$ estimates for (a) the area south of 35°S and split up into sub-sectors, namely (b) the Pacific sector, (c) the Atlantic sector and (d) the Indian sector. The red line in each box center marks the residual median. The blue boxes mark the 25th and 75th percentiles. The whiskers extend to the "extreme values" of the dataset. Individual outliers (outside the whiskers range) are plotted individually as red crosses. (e) number of gridded observations for each sector illustrated as barplots.

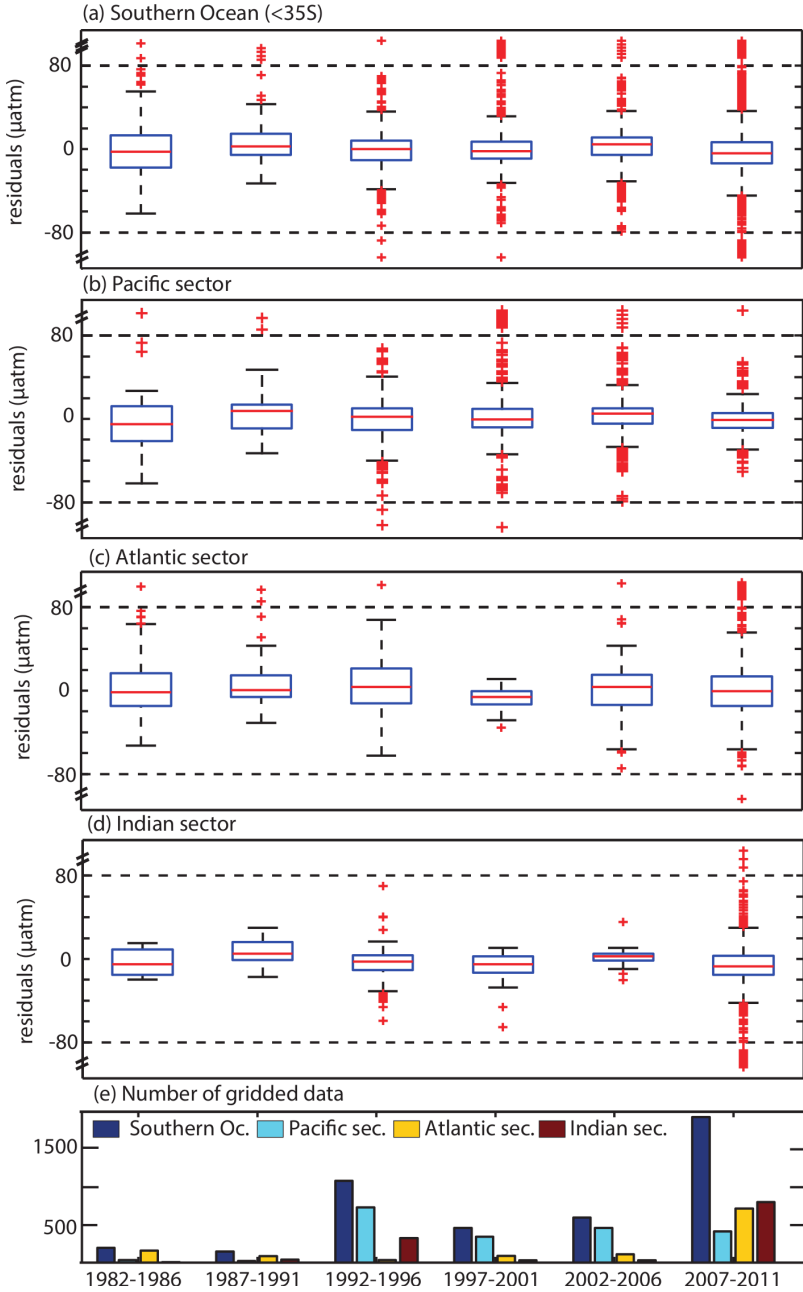


Figure S4: Box-whiskers plot of the residuals between the LDEOv2013 gridded observations that are not included in SOCAT and the neural network $p\text{CO}_2$ estimates for (a) the area south of 35°S and split up into sub-sectors, namely (b) the Pacific sector, (c) the Atlantic sector and (d) the Indian sector. The red line in each box center marks the residual median. The blue boxes mark the 25^{th} and 75^{th} percentiles. The whiskers extend to the "extreme values" of the dataset. Individual outliers (outside the whiskers range) are plotted individually as red crosses.(e) number of gridded observations for each sector illustrated as barplots.

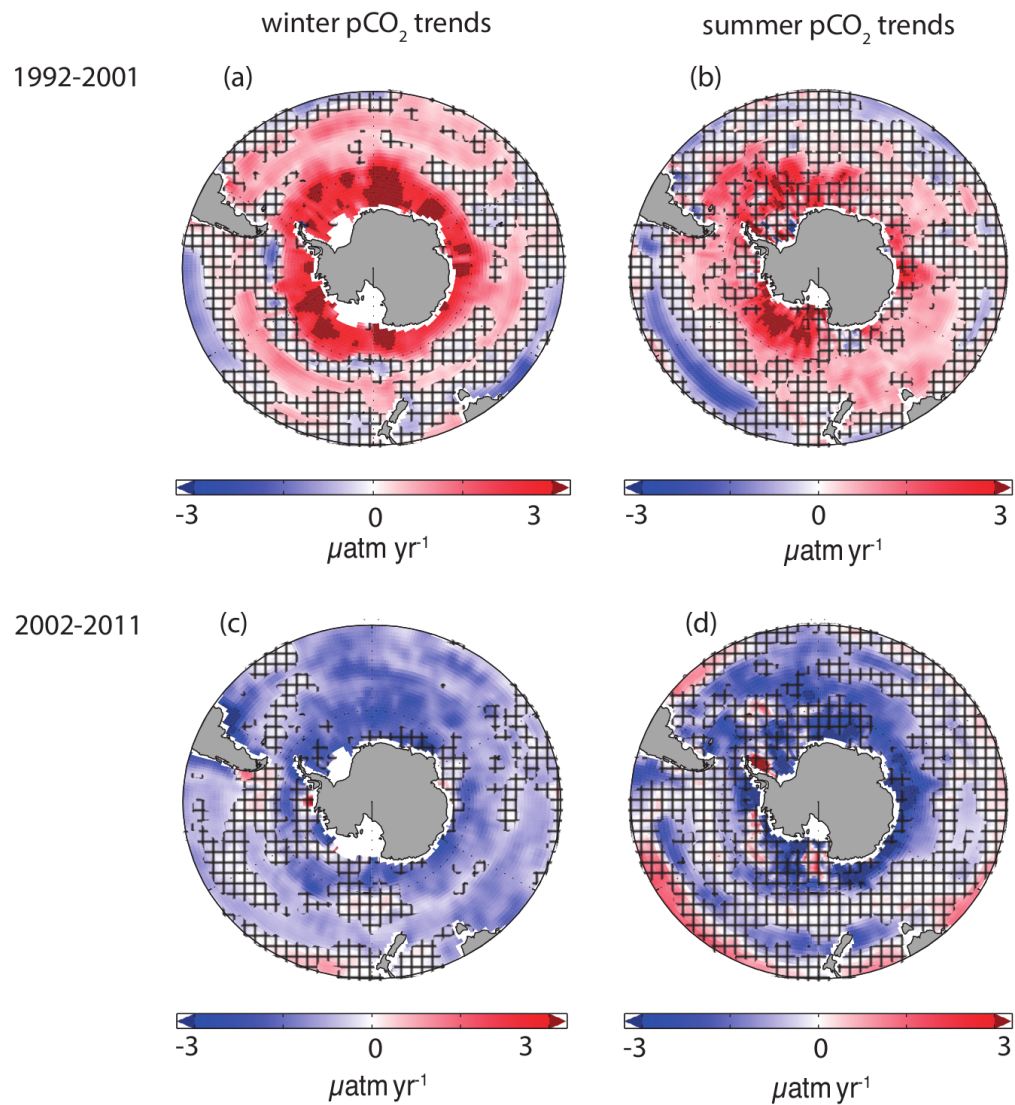


Figure S5: Sea surface $p\text{CO}_2$ trends for the southern hemispheric winter months (JJA) and the southern hemispheric summer months (DJF) from 1992 through 2001 (a-b) and 2002 through 2011 (c-d). Hatched areas indicate where the linear trends are outside the 5% significance level ($p \geq 0.05$).

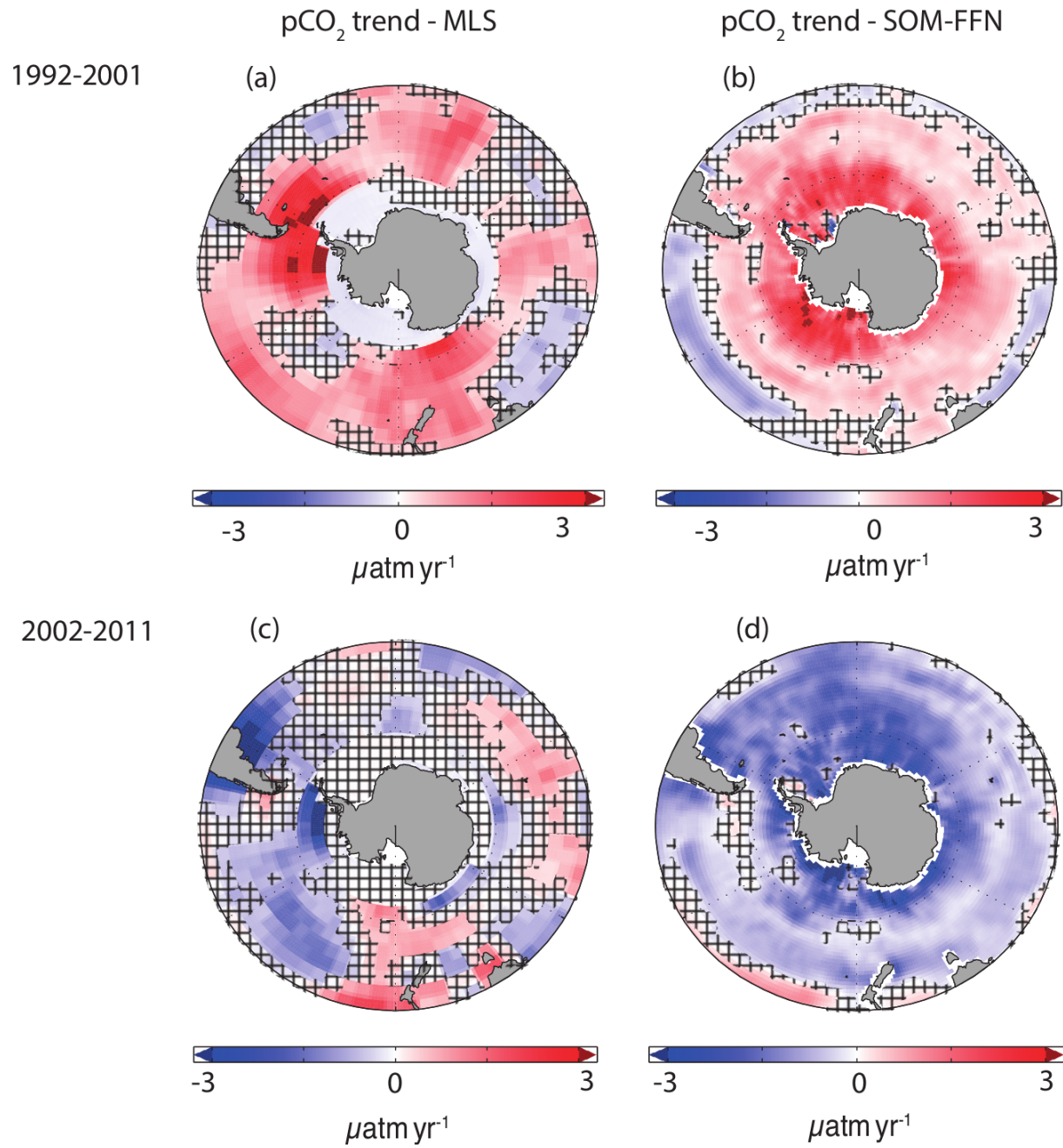


Figure S6: Trends in the sea-surface $p\text{CO}_2$ from 1992 through 2001 (a-b) and 2002 through 2011 (c-d) derived from the mixed layer scheme model in comparison to the SOM-FFN method. Hatched areas indicate where the linear trends are outside the 5% significance level ($p \geq 0.05$)

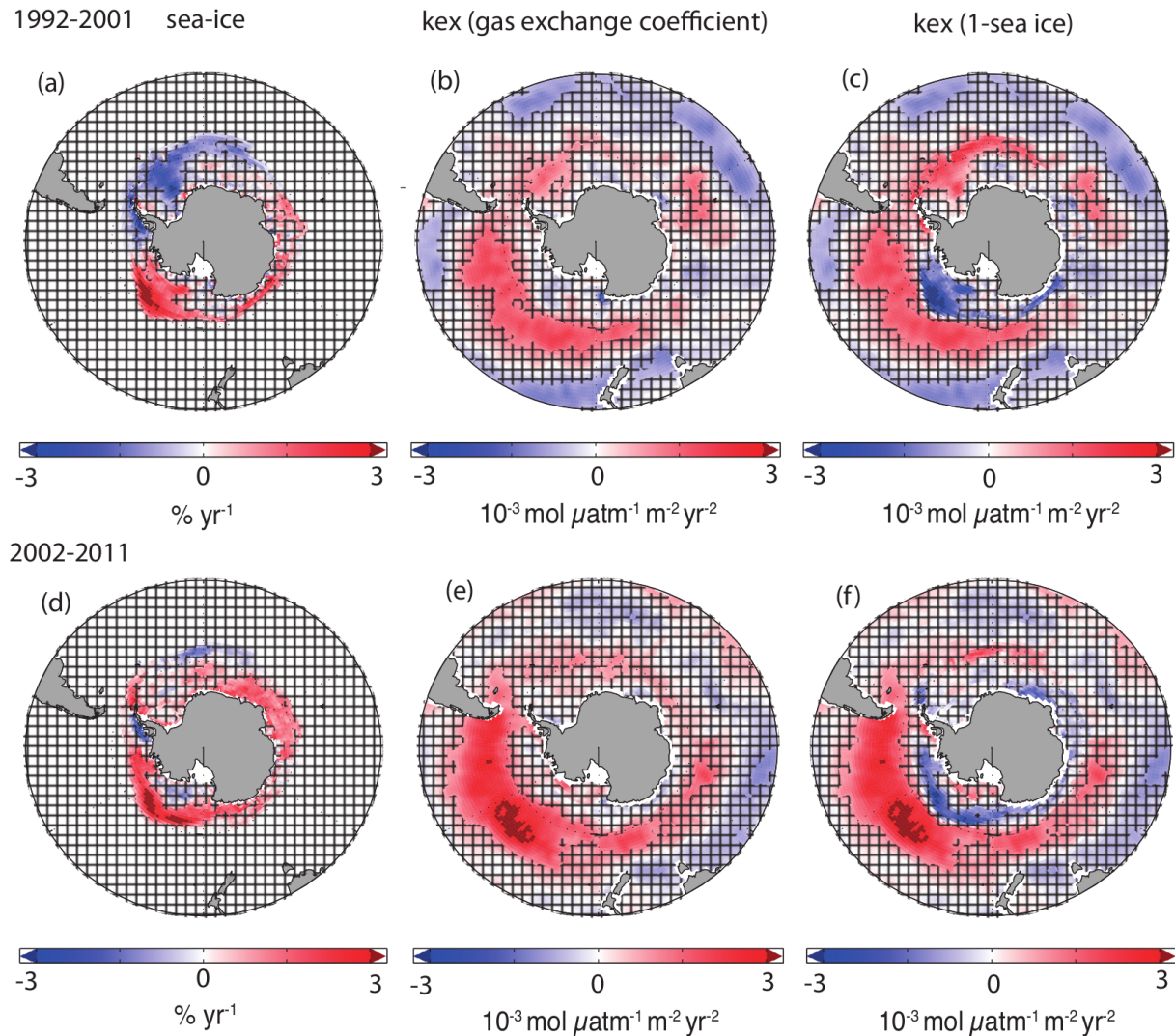


Figure S7: Trends in sea ice extent, the gas transfer coefficient ($k_j \cdot$ solubility) and the combined gas transfer coefficient from 1992 through 2001 (a-c) and 2002 through 2011 (d-f). Hatched areas indicate where the linear trends are outside the 5% significance level ($p \geq 0.05$).

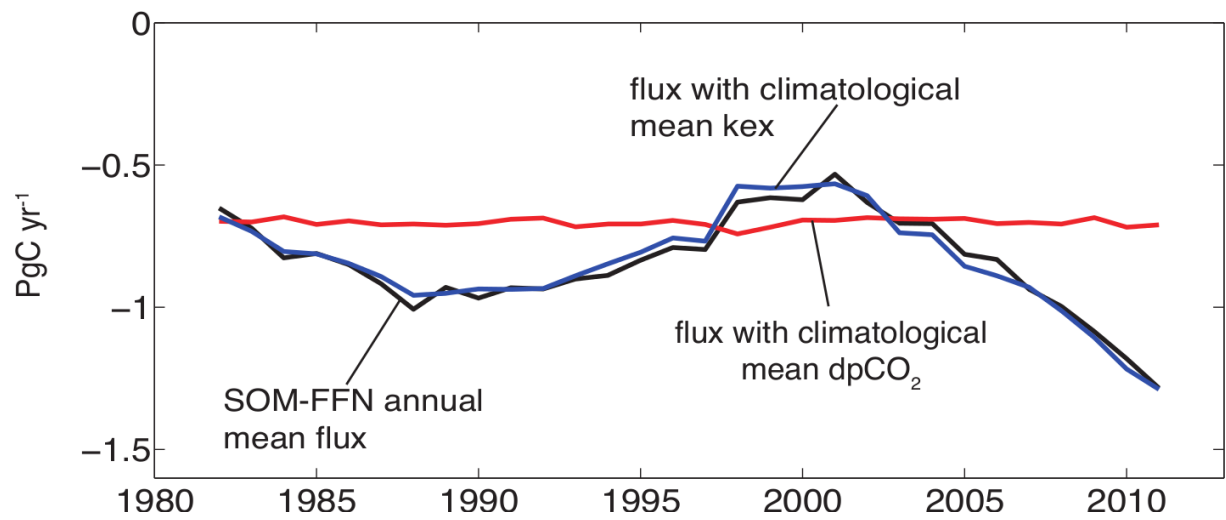


Figure S8: Annual mean carbon uptake in the Southern Ocean south of 35°S. The black line shows the annual integrated carbon uptake from the neural network technique, the blue line shows the uptake based on a constant climatic gas transfer coefficient and constant ice cover (9) ($k_{ex} \cdot [1 - f_{ice}]$) and the red line indicates the Southern Ocean uptake flux with constant climatological ΔpCO_2 . The graph illustrates the dominance of the sea-surface pCO_2 driving the trends discussed in the main manuscript.

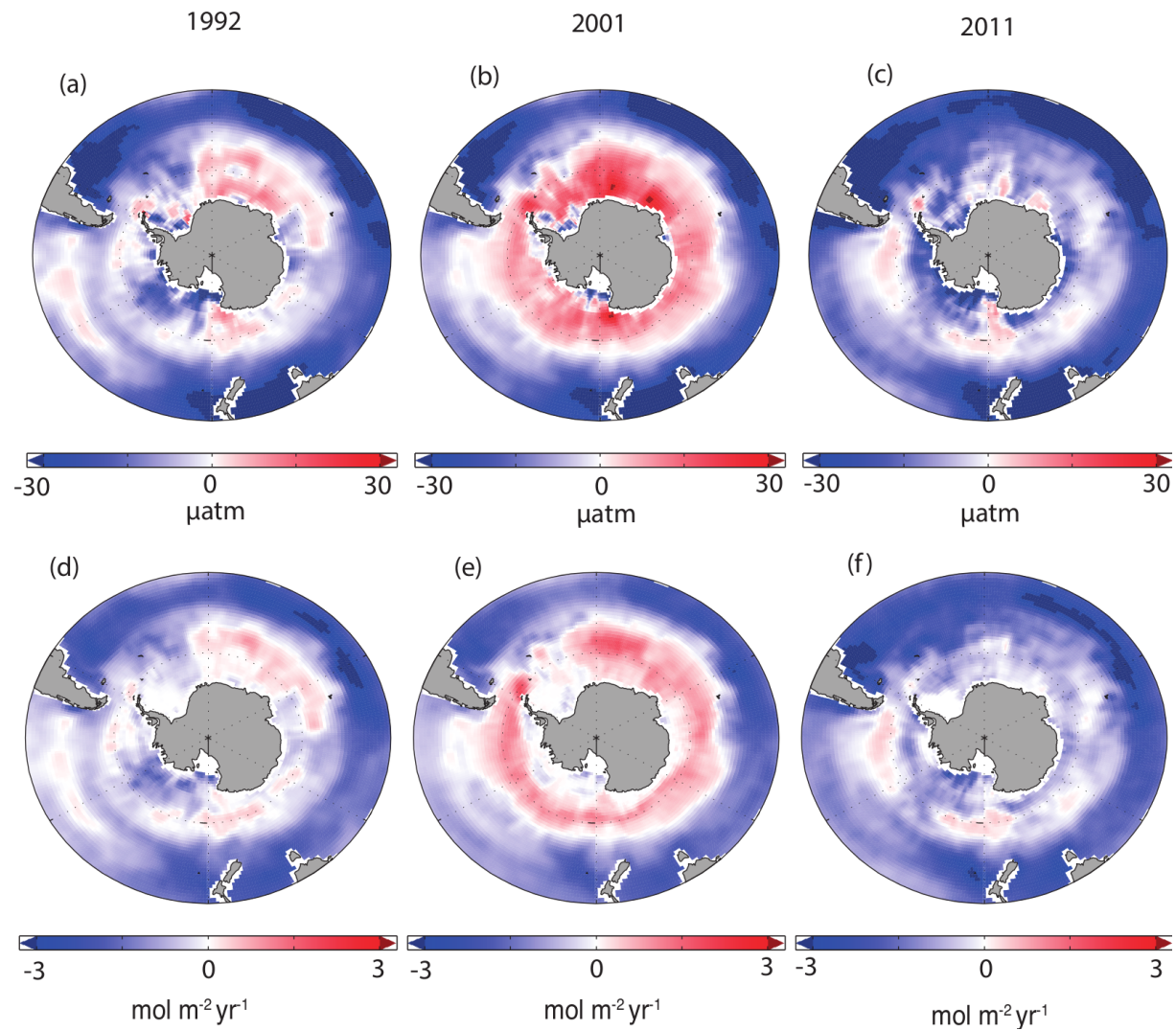


Figure S9: Annual means of the $\Delta p\text{CO}_2$ (a-c) and the air-sea flux density of CO₂ (d-f) for the 3 selected years 1992, 2001 and 2011.

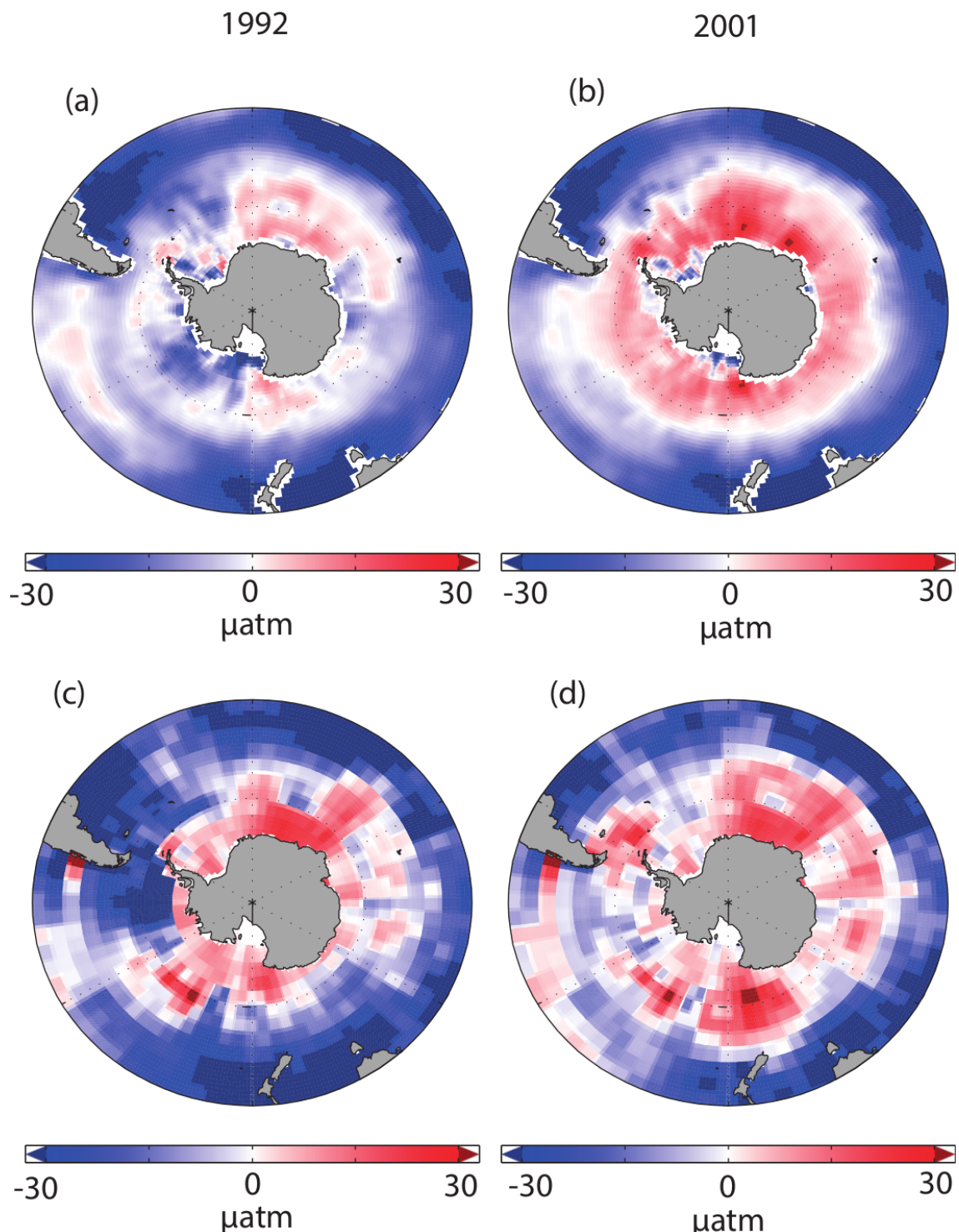


Figure S10: Annual means of the $\Delta p\text{CO}_2$ from the neural network (a-b) in comparison to the mixed-layer scheme (c-d) for 2 selected years 1992 and 2001

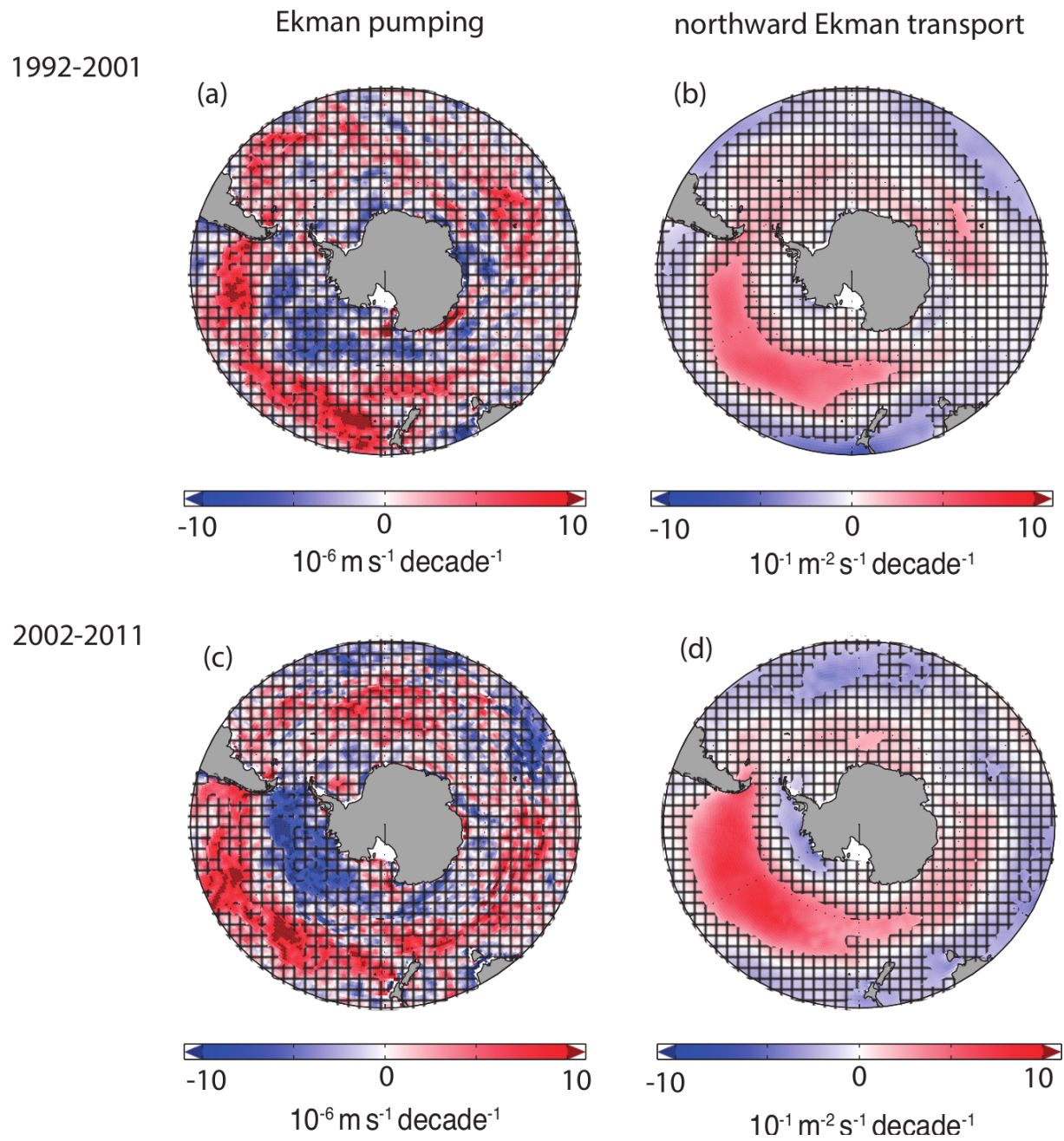


Figure S11: Trends in Ekman pumping w_E and northwards Ekman transport v_E from 1992 through 2001 (a-b) and 2002 through 2011 (c-d). The trends are derived from the monthly mean of the instantaneous surface wind stress components τ^x and τ^y . Hatched areas indicate where the linear trends are outside the 5% significance level ($p \geq 0.05$).

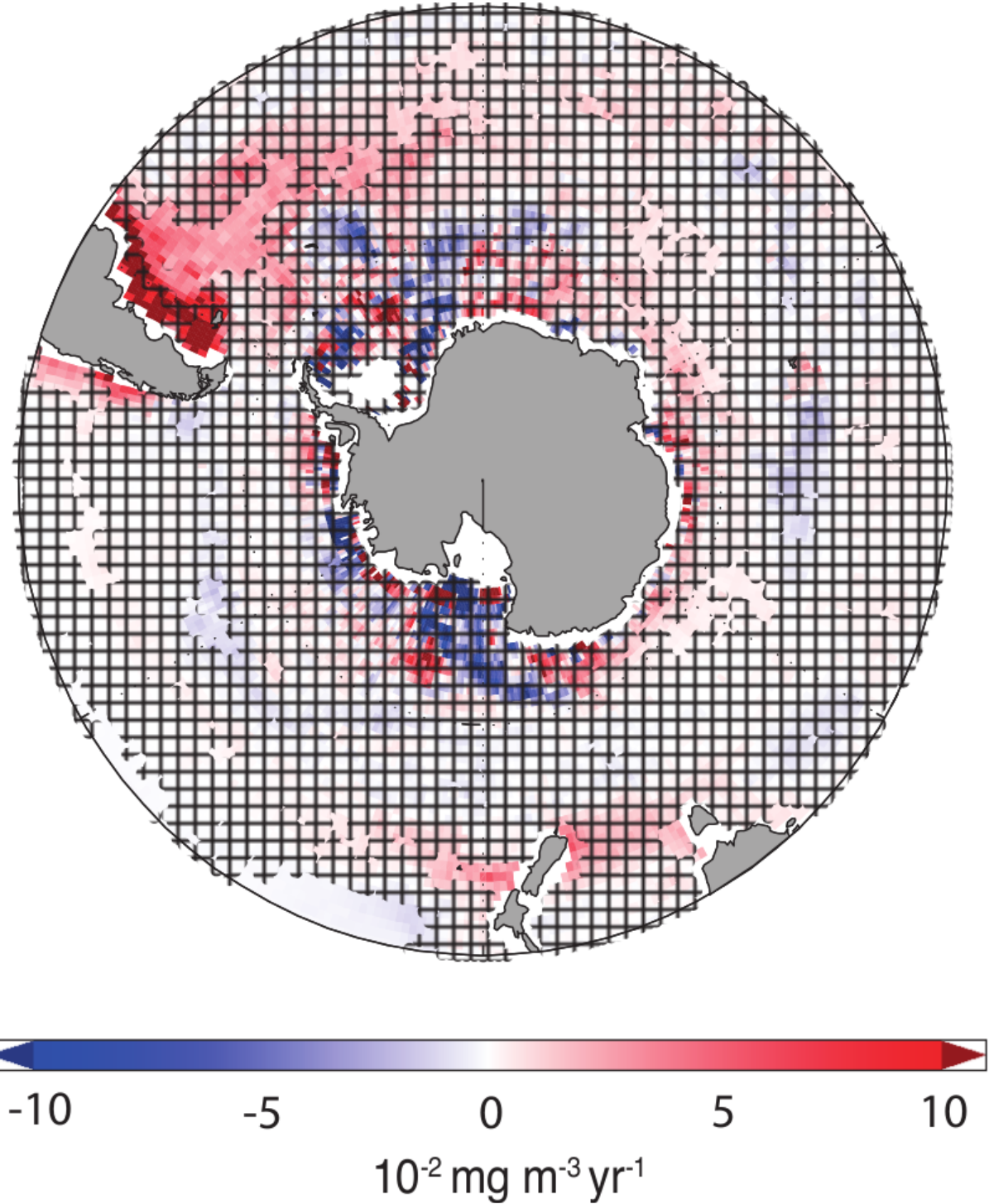


Figure S12: Trends in sea-surface chlorophyll from 2002 through 2011, derived from the Glob-color dataset. Hatched areas indicate where the linear trends are outside the 5% significance level ($p \geq 0.05$).